Assessment of immersed boundary methods for hypersonic flows with gas–surface interactions

Başkaya, Ata Onur; Capriati, Michele; Turchi, Alessandro; Magin, Thierry; Hickel, Stefan

DOI
10.1016/j.compfluid.2023.106134

Publication date
2024

Document Version
Final published version

Published in
Computers and Fluids

Computers and Fluids 270 (2024) 106134

Contents lists available at ScienceDirect

Computers and Fluids

journal homepage: www.elsevier.com/locate/compfluid

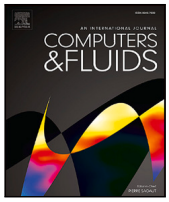

Assessment of immersed boundary methods for hypersonic flows with gas–surface interactions

Ata Onur Başkaya [a,*], Michele Capriati [b,c], Alessandro Turchi [b,d], Thierry Magin [b], Stefan Hickel [a]

[a] Aerodynamics Group, Faculty of Aerospace Engineering, TU Delft, The Netherlands
[b] Aeronautics and Aerospace Department, von Karman Institute for Fluid Dynamics, Belgium
[c] Inria, Centre de Mathématiques Appliquées, Ecole Polytechnique, IPP, France
[d] Science and Research Directorate, Italian Space Agency, Italy

ARTICLE INFO

Keywords:
Immersed boundary method
Mass conservation
Atmospheric entry
Hypersonic flow
Gas–surface interaction
Ablation

ABSTRACT

The efficacy of immersed boundary (IB) methods with adaptive mesh refinement (AMR) techniques is assessed in the context of atmospheric entry applications, including effects of chemical nonequilibrium (CNE) and gas–surface interactions (GSI). We scrutinize a conservative cut-cell IB method and two non-conservative IB methods, comparing their results with analytical solutions, data from the literature, and results obtained with a reference solver that operates on body-fitted grids. All solvers employ the same external thermochemistry library, ensuring that all observed differences can be attributed solely to differences in the underlying numerical methodologies. We present results for eight benchmark cases. Four verification cases verify the implementation of chemistry, transport properties, catalytic boundary conditions, and shock capturing. Four validation cases encompass blunt geometries with adiabatic and isothermal, as well as inert, catalytic and ablative boundary conditions. Overall, the results obtained with the IB solvers are in very good agreement with the reference data. Discrepancies arise in cases with large temperature or concentration gradients at the wall, and these are linked to conservation errors inherent to ghost-cell and interpolation-based IB methods. Only a strictly conservative cut-cell IB method is on par with body-fitted grid methods.

1. Introduction

Hypersonic flows experienced during atmospheric entry of capsules or space debris are characterized by strong shock waves and thermochemical nonequilibrium effects through the excitation of the internal energy modes of species and rapid chemical reactions in the shock layer. The hot gas interacts with the surface thermal protection system (TPS) material installed to protect the spacecraft from this hostile environment. Depending on the characteristics of the TPS material, these gas–surface interactions (GSI) involve catalysis as well as ablation. While the former accelerates the exothermic recombination reactions leading to increased heat transfer towards the surface, the latter alleviates the heat load by means of physicochemical decomposition and mass loss. These ablative GSI change the shape of the object by surface recession. Understanding these interactions is crucial for predicting the surface stresses and heat fluxes, as well as the uncontrolled trajectory of space debris. Ground testing is indispensable for validation purposes; however, no facility can simultaneously replicate all aspects of atmospheric entry flows [1]. Therefore, computational fluid dynamics (CFD) simulations are essential for the aerothermodynamic analysis and design of future spacecraft.

Most CFD solvers used for high-speed and high-enthalpy applications employ body-fitted structured grids [2–4]. In these solvers, alignment of the grid with the shock and the surface needs to be ensured for an accurate prediction of the flow field. Generating these types of grids usually involves strenuous effort from the user especially for detailed features and incremental geometry updates [5]. Unstructured grids have also been explored; however, issues affecting the heat flux predictions at the surface were reported [6,7].

A promising alternative is the use of adaptive mesh refinement (AMR) techniques based on piecewise Cartesian grids with immersed boundary (IB) methods. There has been a recently growing interest in IB-AMR solvers for atmospheric entry applications [8–12], mainly for their potential in considering complex and deforming geometries, and better robustness and higher computational efficiency compared to body-fitted mesh-deformation methods. These methods also allow for a relatively straightforward implementation of high-order schemes. However, special care must be taken to have sufficient grid resolution near the boundaries, as it is more difficult for immersed boundary methods to efficiently resolve thin boundary layers over curved surfaces. To address this shortcoming, a blend of Cartesian grids in the

* Corresponding author.
E-mail address: a.o.baskaya@tudelft.nl (A.O. Başkaya).

https://doi.org/10.1016/j.compfluid.2023.106134
Received 31 August 2023; Received in revised form 4 November 2023; Accepted 23 November 2023
Available online 14 December 2023

fluid and body-fitted grids near the surface can be employed [10,11]. This approach has been successful in reducing the required number of cells and providing better resolution of the thermal boundary layer. In general, a blended grid approach is well suited for shapes with smooth curvatures. However, it is susceptible to the same drawbacks inherent to body-fitted grids, for instance, their difficult adaptation to complex deforming geometries.

Arslanbekov et al. [8], Sekhar and Ruffin [9], and more recently Brahmachary et al. [12] demonstrated the benefits of using IB-AMR solvers for a number of relevant cases. These studies have generally indicated good predictions for wall pressure and skin friction distributions, while emphasizing the difficulty in accurately predicting wall heat fluxes. As with more recent contributions [10,11], these studies were mostly performed with ghost-cell methods from the family of discrete forcing IB approaches [13]. Ghost-cell methods impose boundary conditions by interpolating or extrapolating the fluid solution within a narrow region at the interface, i.e. into ghost cells that are used by the baseline scheme for updating the neighboring fluid cells. Relying solely on ghost cells does not ensure strict conservation of mass, momentum, and energy if the interface is not aligned with the Cartesian mesh. A strictly conservative approach is the cut-cell finite-volume method, which splits fluid and solid domains into consistently deformed finite volumes. The implementation of a cut-cell method for three dimensions and high-order schemes is not as straightforward as the ghost-cell approach, and it also introduces additional challenges such as cut-cells with very small fluid volumes. However, the main advantage of the cut-cell method lies in satisfying the conservation of mass, momentum, and energy near the wall [13].

In this paper, ghost-cell and cut-cell IB methods are scrutinized through a curated list of benchmark case studies relevant for atmospheric entry applications. The main aim of this paper is twofold:

- to assess the accuracy of IB methods for applications with strong thermal gradients and gas–surface interactions,
- to establish a set of well-defined test cases for the verification and validation of IB methods for atmospheric entry.

Results obtained with the IB-AMR solvers INCA [14,15] and CHESS [16,17] are compared to reference results obtained with the body-fitted finite-volume solver US3D [6] in addition to data from literature. A consistent assessment of the accuracy of the numerical methods is achieved by coupling all three flow solvers with the same thermochemistry library, Mutation^{++} [18], which ensures that any discrepancy in the results can be attributed solely to differences in the underlying numerical methodologies.

The paper is structured as follows: Governing equations and modelling approaches are presented in Section 2. Solver methodologies are introduced in Section 3. Results of the benchmark case studies are presented and discussed in Section 4, while the influence of the different IB methodologies is further investigated in Section 5. Concluding remarks are made in Section 6.

2. Governing equations and models

2.1. Governing equations

The compressible Navier–Stokes equations are solved in their conservative form for a reacting multicomponent fluid,

$$\frac{\partial \rho_i}{\partial t} + \boldsymbol{\nabla} \cdot \left(\rho_i \mathbf{u}\right) + \boldsymbol{\nabla} \cdot \mathbf{J}_i = \dot{\omega}_i \,, \tag{1}$$

$$\frac{\partial \rho \mathbf{u}}{\partial t} + \boldsymbol{\nabla} \cdot (\rho \mathbf{u} \otimes \mathbf{u}) + \boldsymbol{\nabla} p - \boldsymbol{\nabla} \cdot \boldsymbol{\tau} = 0 \,, \tag{2}$$

$$\frac{\partial \rho E}{\partial t} + \boldsymbol{\nabla} \cdot \left[(\rho E + p)\,\mathbf{u}\right] + \boldsymbol{\nabla} \cdot \mathbf{q} - \boldsymbol{\nabla} \cdot (\boldsymbol{\tau} \cdot \mathbf{u}) = 0 \,, \tag{3}$$

where ρ_i is the species partial density for the i^{th} species, $\mathbf{u}$ is the mixture average velocity, $\dot{\omega}_i$ is the source term associated with the production or consumption of species due to chemical reactions, ρ is the mixture density, p is the mixture pressure, and $E = e + u^2/2$ is the specific total energy, which is the sum of the thermodynamic internal energy e and the kinetic energy. External forces due to gravitational or electromagnetic effects, and radiative energy exchanges are not considered for the cases in this study. The solvers considered in this work can perform under thermal nonequilibrium with multi-temperature methods, such as that of Park [19]. However, results presented in this paper are obtained with a thermal equilibrium assumption.

The ideal gas assumption leads to the equation of state $p = \rho R T$, where T is the temperature and $R = \mathcal{R}/\overline{M}$ is the mixture gas constant obtained from the universal gas constant $\mathcal{R}$ and the mixture average molar mass $\overline{M}$. These mixture properties are modeled according to Dalton's law through their constituent species as $p = \sum_i p_i$, $\rho = \sum_i \rho_i$, $R = \sum_i y_i R_i$, with the mass fractions $y_i = \rho_i/\rho$.

Two models are considered for the species diffusion flux $\mathbf{J}_i$: Fick's law with a correction to ensure conservation of mass is

$$\mathbf{J}_i = -\rho D_{im} \boldsymbol{\nabla} y_i + y_i \sum_j \rho D_{jm} \boldsymbol{\nabla} y_j \,, \tag{4}$$

with the mixture-averaged $D_{im} = (1 - x_i) \Big/ \sum_{j \neq i} x_j / \mathscr{D}_{ij}$ obtained by Wilke's average of the binary diffusion coefficients $\mathscr{D}_{ij}$. The second diffusion model uses the solution of the Stefan-Maxwell equations,

$$\boldsymbol{\nabla} x_i = \frac{\overline{M}}{\rho} \sum_{j \neq i} \left(\frac{x_i \mathbf{J}_j}{M_j \mathscr{D}_{ij}} - \frac{x_j \mathbf{J}_i}{M_i \mathscr{D}_{ij}} \right) \,, \tag{5}$$

where x_i are the mole fractions, and M_i are the species molar masses. This formulation is computationally costlier, but theoretically more accurate [20].

Viscosity and thermal conductivity are obtained through a linear system solution using an LDL$^{\mathrm{T}}$ decomposition as opposed to the common approach of using simplified mixture rules [21–23]. The viscous stress tensor $\boldsymbol{\tau}$ is defined assuming Stokes' hypothesis as

$$\boldsymbol{\tau} = \mu \left[\boldsymbol{\nabla} \mathbf{u} + (\boldsymbol{\nabla} \mathbf{u})^{\dagger} - \frac{2}{3} \boldsymbol{\nabla} \cdot \mathbf{u} \boldsymbol{I} \right] \,, \tag{6}$$

where μ is the dynamic (shear) viscosity of the mixture. The total heat flux vector

$$\mathbf{q} = -\lambda \boldsymbol{\nabla} T + \sum_i \mathbf{J}_i h_i(T) \tag{7}$$

includes the contributions from conduction and mass diffusion. The first term stems from Fourier's law with the thermal conductivity λ of the mixture, and the second term accounts for the transport of enthalpy by species diffusion, with h_i as the species enthalpy.

2.2. Physicochemical modelling

The models used in state-of-the-art CFD solvers capable of simulating the aforementioned hypersonic flow phenomena vary considerably. Broadly, choices need to be made on the thermodynamic database, the treatment of TCNE effects, the transport properties modelling, and the approach for handling GSI. For details we refer to several published studies that evaluate the impact of these selections in modelling thermal nonequilibrium [24,25], species diffusion [20,26], viscosity and thermal conductivity [26,27], rate of catalysis [28], and ablation [29]. As important quantities of interest, such as surface heat fluxes, are highly sensitive to modelling details, large discrepancies between the results obtained with hypersonic CFD codes are common [3,4], and the variety of models often obscures a clear assessment of the underlying numerical methods, when comparing different solvers. Based on these considerations, the CFD solvers used in this study have been coupled with the multicomponent thermodynamic and transport properties for ionized gases in C++ (Mutation^{++}) open-source library. Mutation^{++} provides all required physicochemical models for thermodynamics, transport properties, chemical kinetics, and GSI. A detailed description of Mutation^{++} is presented by Scoggins et al. [18].

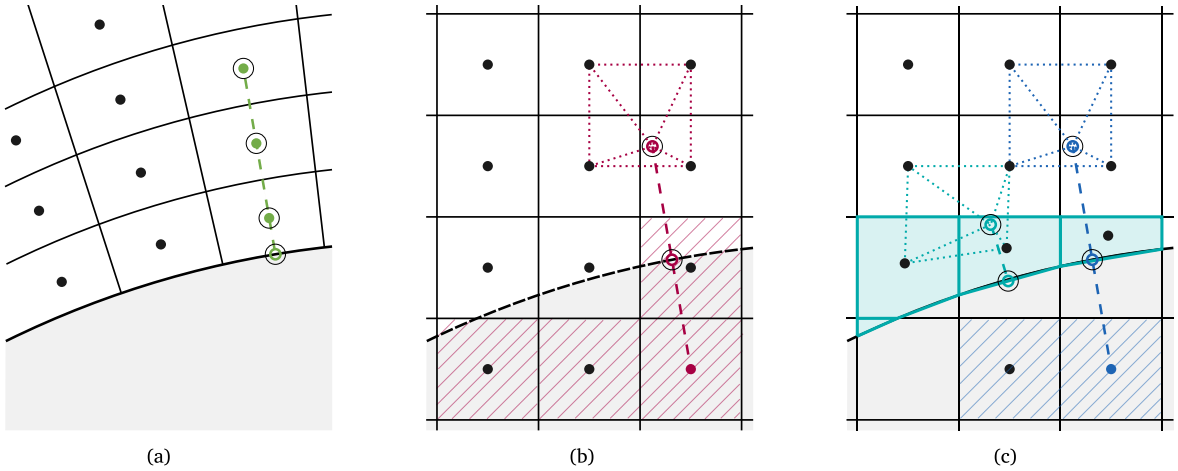

Fig. 1. Schematics of (a) body-fitted (green), (b) ghost-cell IB, and (c) cut-cell IB approaches. Ghost cells are hatched (violet or blue) and cut-cells are tinted (turquoise).

The caloric properties of the species are approximated with standard NASA-9 polynomial fits [30]. Species mass diffusivities, viscosities, and thermal conductivities are provided by Mutation^{++} according to multi-component Chapman–Enskog formulations [31]. The chemical reaction mechanisms, that is, species mass rates and their analytical Jacobians with respect to species densities, are also provided by Mutation^{++}.

Catalytic and ablative surface boundary conditions are imposed by solving a mass balance [18,32],

$$(\rho_i v_{blow})_{wall} + (J_i)_{wall} = \dot{\omega}_{i,wall} \,, \tag{8}$$

with v_{blow} as the surface-normal blowing velocity, which is nonzero only for an ablative boundary. Terms from left to right refer to convective flux due to blowing, diffusive flux, and species source term due to surface reactions. A probability based approach is employed for computing this chemical source term for the surface, written as

$$\dot{\omega}_{i,wall} = \gamma m_i \mathcal{F}_{i,impin} \,, \tag{9}$$

where $\gamma = \mathcal{F}_{i,react}/\mathcal{F}_{i,impin}$ is the ratio of reacting to impinging species fluxes and it describes the efficiency of the process, and m_i is the mass of the ith species [32]. Assuming the species at the wall have a Maxwellian distribution function, the impinging species flux is

$$\mathcal{F}_{i,impin} = n_i \sqrt{\frac{k_B T_w}{2\pi m_i}} \,, \tag{10}$$

where k_B is the Boltzmann constant, T_w is the wall temperature, and n_i is the number density of the i^{th} species [33]. From the mass blowing rate $\dot{m} = \sum_i \dot{\omega}_{i,wall}$, the blowing speed is calculated by

$$v_{blow} = \frac{\dot{m}}{\sum_i \rho_i} \,. \tag{11}$$

Values obtained for species densities and mass blowing speeds are then imposed as boundary conditions for the Navier–Stokes equations.

3. Numerical methods

We consider three different methodologies for imposing surface boundary conditions in the framework of finite-volume methods. Schematics of the body-fitted, ghost-cell IB, and cut-cell IB approaches are shown in Fig. 1. The arc near the middle of each sketch indicates the surface that demarcates the fluid above from the solid below it. The other black lines are grid lines and the filled dots indicate cell centers. The color code matches the one used for presenting the results obtained with these methods in Section 4.

The classical body-fitted grid method, Fig. 1(a), simply makes use of the grid's alignment with the geometry. The fluid-cell solutions and boundary conditions are used to reconstruct quantities at cell interfaces according to the chosen numerical scheme. An example stencil is drawn in the sketch and the boundary intercept is indicated by a colored hollow circle. Hollow circles indicate the stencil of the discretization scheme.

The two other approaches use IB methods on Cartesian grids. Ghost-cell IB approaches, sketched in Fig. 1(b), impose boundary conditions through a virtual flow solution in ghost cells, which is obtained by interpolation from the surrounding fluid-cell solutions and the boundary conditions at the nearest fluid–solid interface. For ghost cells that are outside of the fluid domain, the interpolation is performed at a mirrored image point [34]. An example stencil is shown in the sketch, with the fluid points used in the interpolation at the image point connected by dotted lines. Different criteria can be used for defining the set of ghost cells: some methods select ghost cells based on their cell-center coordinate within the solid (solid cells hatched in the sketch) [34], whereas other methods include cells that are cut by the interface or have a neighbor within the solid (so-called interface cells) [35]. While being relatively straightforward to implement, this approach does not ensure strict conservation of mass, momentum, and energy at the interface between the fluid and the solid. Fluxes are reconstructed from the fluid-cell and the ghost-cell solutions on the Cartesian grid without considering the location and shape of the fluid–solid interface. Errors in implicitly satisfying the conservative flux boundary condition therefore result from the nonlinearity of the flux function, from the image point interpolation, and from the interface curvature.

The cut-cell IB approach [36–38], see Fig. 1(c), ensures strict conservation of mass, momentum, and energy by considering the flux balance for the part of the cell that belongs to the fluid domain. These consistently deformed finite volumes and their cell faces are colored in the sketch. Fluxes over the cell faces of the cut cells are scaled according to the wetted areas. The exchange of mass (e.g. with surface reactions), momentum, and energy through the fluid–solid interface is calculated from the prescribed boundary conditions and the local fluid solution. The latter is acquired by interpolation from the surrounding cell values and the boundary conditions. An example stencil is colored in the sketch for the cut-cell interpolation. The other stencil in the sketch is identical to the ghost-cell IB approach. This addition to the cut-cell method refers to the specific implementation within the INCA solver and will be discussed in Section 3.2. Cut-cells with a very small fluid volume fraction require a special treatment to ensure stable time integration. They are typically mixed or merged with nearby cells [38].

3.1. Body-fitted solver

The body-fitted solver considered in this study is US3D, which is a high-fidelity flow solver specifically designed for aerodynamic applications in the hypersonic regime by the University of Minnesota and

NASA [6]. It solves the compressible chemically reacting Navier-Stokes equations in a finite-volume framework on unstructured body-fitted grids. Among the several numerical schemes available in the solver, all simulations carried out within this work use the modified Steger–Warming scheme [39], which is suitable for steady computations. A MUSCL approach [40] is employed to obtain second-order accurate fluxes. Both explicit and implicit time integration methods are available; in this work, rapid convergence to steady state is achieved with the data parallel line relaxation (DPLR) method [41]. US3D is equipped with chemistry/multi-temperature source terms and transport properties with the possibility to account for high temperature and high pressure effects. Native routines can be further extended by user-defined subroutines, which allow coupling the solver to external libraries; we refer to Capriati et al. [42] for the coupling with Mutation^{++}.

3.2. Immersed boundary solvers

Two IB solvers are considered: one able to use both the cut-cell and the ghost-cell methods, and another using only the latter.

Employing a cut-cell IB methodology, INCA is a high-fidelity finite-volume solver for direct numerical simulations (DNS) and large eddy simulations (LES) of the compressible chemically reacting Navier–Stokes equations and provides a large number of different discretization schemes on block-Cartesian AMR grids [14,15]. For the purposes of this study, a third-order weighted essentially non-oscillatory (WENO) scheme [43] with HLLC flux function [44] is selected to discretize the inviscid terms. WENO schemes permit high accuracy in smooth regions, while ensuring stable and sharp capturing of discontinuities. Second-order central differences are used for the viscous terms and the explicit third-order Runge–Kutta scheme of Gottlieb and Shu [45] is selected for time integration. Chemical source terms are treated using Strang's second-order time splitting scheme [46] to alleviate the numerical stiffness caused by these terms. The chemical source terms thus reduce to a system of ordinary differential equations, which is solved by the VODE library [47]. INCA employs a unique improvement to the common cut-cell methodology [38], which we refer to as the cut-element method [48,49]. This method represents the fluid–solid interface through cut-elements, which are derived from the Cartesian mesh and the triangulation of the surface geometry. Instead of considering a planar intersection of a finite-volume cell with the wall surface, as typically done in cut-cell methods [50,51], cut-elements maintain all details of the intersection of the grid with the surface triangulation. The interface within each cut-cell is thus represented by several cut-elements belonging to different surface triangles to yield sub-cell accuracy and robustness for complex geometries. This method is a consistent and conservative extension of the finite volume flux balance to accommodate cells that are divided by boundaries. Further details on this cut-element methodology and its extension to incorporate GSI and thermal nonequilibrium are provided in Ref. [52].

INCA utilizes ghost cells to enable the use of unmodified stencils across the entire domain. Furthermore, the cut-cell procedure that guarantees strict conservation can be deactivated, leaving the immersed boundary solely represented by the extrapolated virtual flow solution in ghost cells. We will discuss results obtained with this INCA ghost-cell method for selected cases in Section 5.

In contrast to INCA, the IB method implemented in the flow solver CHESS of Politecnico di Bari [17] fully relies on interpolation in interface cells. The numerical method utilized by CHESS is based on the flux vector splitting proposed by Steger and Warming [39] with a second-order MUSCL reconstruction in space [40] for the hyperbolic terms. Discretization of the viscous fluxes uses Gauss's theorem in conjunction with a second-order linear reconstruction of the solution. A third-order explicit Runge–Kutta scheme is employed for time integration of the transport terms in the Navier–Stokes equations. Following the Runge–Kutta time step, chemical source terms are computed by means of a Gauss–Seidel scheme. The IB method of CHESS is also combined with AMR to provide appropriate resolution of shocks and boundary layers [35] and uses the same physicochemical models as US3D and INCA [16]. Further details on the solver can be found in the aforementioned works.

4. Benchmark cases

We have curated a set of benchmark cases through collaborative effort with several research groups [16]. The goal is to first verify the physicochemical models and the numerical schemes. Once confidence is established over these fundamental aspects, the accuracy and limitations of the IB methods is addressed. We have selected setups that are sufficiently challenging for the methods under assessment, and simple enough to be readily reproduced by others to incentivize collaboration. For IB methods on Cartesian grids, curved geometries were selected to include the entire angular range of fluid–solid interfaces in two dimensions. These cases include strong thermal gradients near cold isothermal walls as well as gas–surface interactions such as catalytic reactions and ablative surface blowing.

The benchmark cases are summarized in Table 1. The first four cases verify the correct implementation of key solver components, such as chemistry, transport properties, the catalytic boundary conditions, and the numerical schemes for shock capturing. Established validation experiments are chosen as the final benchmark cases: the fifth, sixth and seventh cases are 2-D cylinder flows of Knight et al. [3] with inert adiabatic, inert isothermal, and catalytic isothermal surfaces. The eighth benchmark case is an ablative TPS sample geometry under plasma wind tunnel conditions, for which reference experimental data is provided by Helber et al. [53].

4.1. 0-D reactor

The first study verifies the chemical source term implementation by considering 5-species air, $[N_2, O_2, NO, N, O]$, in an adiabatic reactor. Starting from the chemical nonequilibrium (CNE) initialization provided in Table 2, the system is left free to time-march towards the equilibrium state according to chemical mechanisms from Park [54,55]. The solutions provided by all three solvers are shown in Fig. 2. Dissociation of N_2, O_2 and the resulting formation of NO, N, and O can be seen. The code-to-code agreement is excellent.

4.2. 1-D diffusion problem

This test case verifies the implementation of models for transport properties. Viscosity and thermal conductivity are obtained through

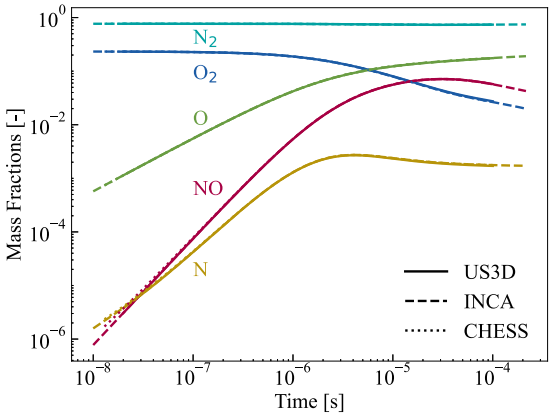

Fig. 2. Evolution of mass fractions for 5-species air in the 0-D reactor case.

Table 1
Summary of studied cases.

	Name	Aspect to assess	Section
1.	0-D Reactor	Chemistry	4.1
2.	1-D Diffusion problem	Mass diffusion	4.2
3.	1-D Catalytic diffusion problem	Mass diffusion with catalysis	4.3
4.	1-D Shocktube	Shock capturing	4.4
5.	2-D Cylinder (inert, adiabatic wall)	Chemical nonequilibrium	4.5.1
6.	2-D Cylinder (inert, isothermal wall)	Surface heat flux	4.5.2
7.	2-D Cylinder (fully catalytic, isot. wall)	Surface heat flux with catalysis	4.5.3
8.	2-D Ablator	Surface mass blowing with ablation	4.6

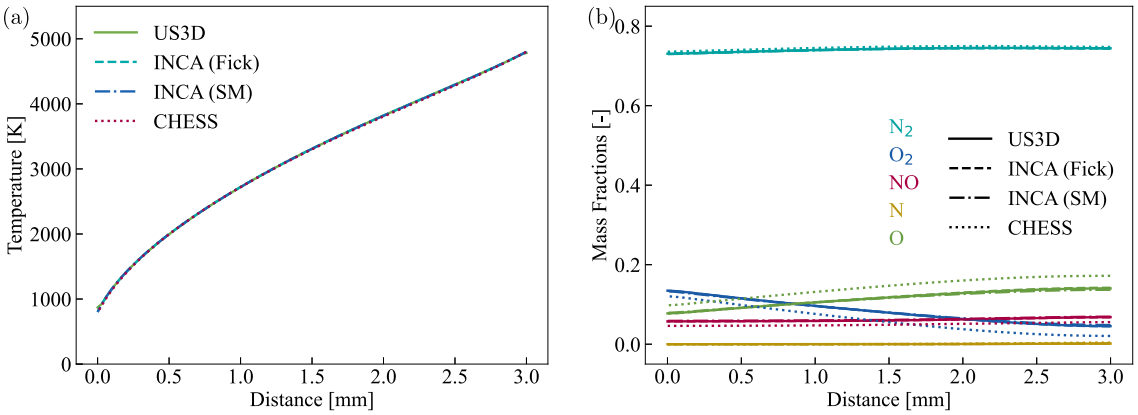

Fig. 3. Comparison of (a) temperature and (b) mass fraction distributions for the 1-D diffusion case.

Table 2
Setup conditions for the 0-D reactor case.

ρ [kg/m^3]	T [K]	u [m/s]	$y(N_2)$	$y(O_2)$
0.01	7000	0.0	0.767	0.233

Table 3
Setup conditions for the 1-D diffusion case.

ρ [kg/m^3]	T [K]	T_{left} [K]	T_{right} [K]	u [m/s]	$y(N_2)$	$y(O_2)$
0.02	1000	800	4800	0.0	0.767	0.233

direct calls to Mutation^{++}, and are exactly equal for all solvers. Therefore, mainly the differences in the implementation of the driving force and boundary conditions are assessed. The setup consists of a 1-D tube with isothermal end walls at different temperatures. The initial and boundary conditions are provided in Table 3. The mixture composition and reaction mechanisms are the same as in the 0-D reactor case. The tube is 3 mm long. It should be pointed out that the computational meshes in US3D and INCA solvers have 100 cells, whereas CHESS results [16] used 400 cells. It has been verified that the US3D and INCA solutions are grid converged on the mesh with 100 cells.

In this test case the temperature gradient leads to chemical reactions, which in turn drive mass diffusion. Temperature and mass fraction distributions along the tube are presented in Fig. 3. INCA results have been obtained by both Fick's law and Stefan–Maxwell diffusion models. However, for this test case, differences seem to be negligible between the two. Overall, US3D results are matched perfectly with INCA, while slight differences are observed for the mass fraction distributions predicted by CHESS, even though the temperature profiles match exactly.

4.3. 1-D catalytic diffusion problem

This test case verifies the catalytic boundary condition implementation for a simple [N_2, N] binary mixture along a 1-D tube, for which an analytical solution exists and is derived in the Appendix. Setup

Table 4
Setup conditions for the 1-D catalytic diffusion case.

p [Pa]	T [K]	T_{wall} [K]	u [m/s]	$y(N_2)$	$y(N)$	γ_N
100	3000	3000	0.0	0.0	1.0	[0.001, 0.01, 0.1, 1.0]

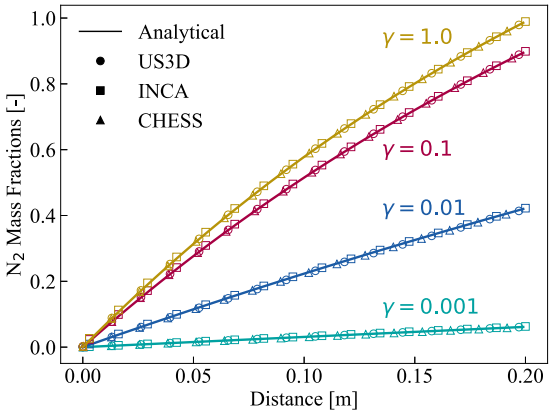

Fig. 4. N_2 mass fractions for different recombination coefficients γ for the 1-D catalytic diffusion case.

conditions are given in Table 4. The length of the tube is 0.2 m. One side of the tube at x = 0.0 m is at reservoir conditions, while at the other, at x = 0.2 m, a catalytic wall boundary condition is imposed. The catalytic wall promotes the recombination of nitrogen $N + N \rightarrow N_2$. The reaction rate is controlled by the recombination coefficient γ, see Eq. (9).

Results obtained with US3D, INCA, and CHESS [16] are compared with the analytical reference solution in Fig. 4. Naturally, the mass fraction of molecular nitrogen at the wall increases for higher values of the recombination coefficient γ, and reaches unity for the fully catalytic case with $\gamma = 1.0$. All numerical predictions are in excellent agreement with the analytical solution. The previously noted difference for the

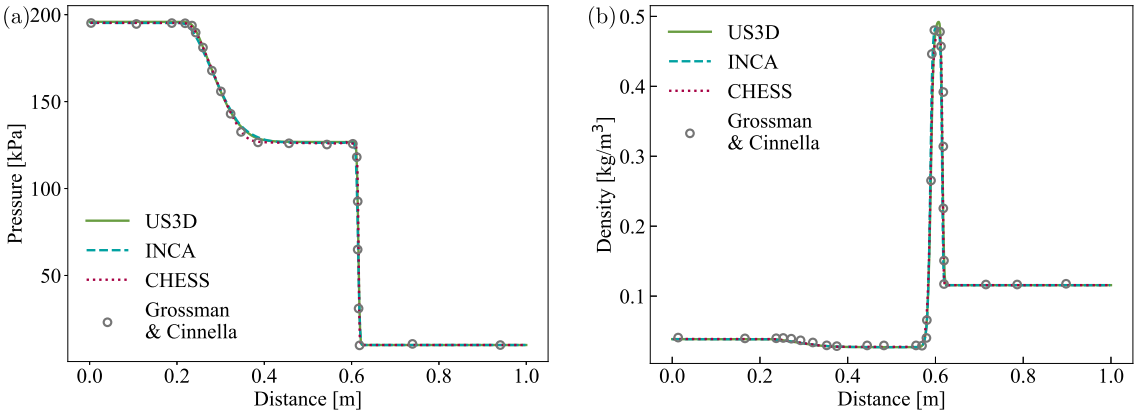

Fig. 5. Comparison of (a) pressure and (b) density distributions for the 1-D shocktube case of Grossman and Cinnella [56].

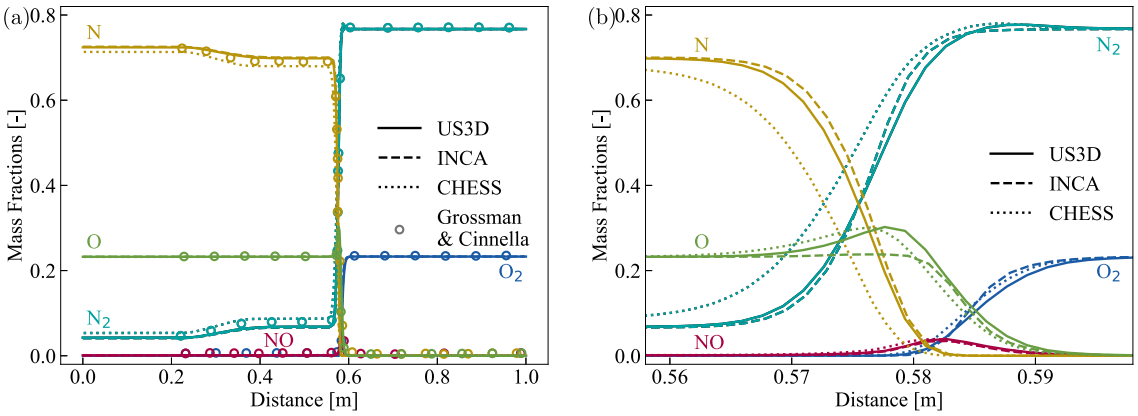

Fig. 6. Comparison of mass fraction distributions for the 1-D shocktube case of Grossman and Cinnella [56].

CHESS solver in the diffusion problem is not observed here as the diffusion of species are driven predominantly by the surface reactions.

4.4. 1-D shocktube

The Riemann problem of Grossman and Cinnella [56] is used to evaluate shock capturing. The unit domain, x = [0, 1] m, is spatially discretized by 600 cells, in line with the reference resolution. The diaphragm separating the two initial states is set at the midpoint of the tube. The initial conditions for the two states are given in Table 5. Air with 5-species is initially considered at thermodynamic equilibrium. The reaction mechanism is taken from an earlier work of Park [57], to match with Ref. [56]. Grossmann and Cinnella applied a thermal nonequilibrium model; however, we have performed tests with Park's two-temperature model [19] and found no significant differences between the translational and vibrational energy modes. Therefore, we show results that have been obtained with a thermal equilibrium assumption.

Fig. 5 shows pressure and density profiles 99 μs after the initial state. Mass fractions are given in Fig. 6. The contact discontinuity and the shock wave traveling in the positive x direction as well as the expansion traveling in the opposite direction are well captured by all solvers. The peak in density after the shock also matches perfectly with the reference results without any oscillations. Predictions of US3D and INCA for the mass fractions are also in excellent agreement with the reference results of Grossmann and Cinnella, see Fig. 6a. The minor differences between the solvers in their sharp representation of the discontinuity is shown in the close-up view in Fig. 6b. CHESS [16] predicts a slightly higher N_2 mass fraction, and accordingly less atomic nitrogen, than US3D and INCA.

Table 5
Initial conditions for the 1-D shocktube case.

u_{left} [m/s]	T_{left} [K]	p_{left} [Pa]	u_{right} [m/s]	T_{right} [K]	p_{right} [Pa]
0.0	9000	195 256	0.0	300	10 000

4.5. 2-D cylinder

2-D cylinder flows are used for the validation of surface heat flux calculations under inert and catalytic wall conditions. Knight et al. [3] have presented an assessment of five different CFD codes from participating institutions with respect to reference experiments conducted at the high-enthalpy shock tunnel of the German Aerospace Center (DLR) [58]. The experiment investigates the flow past a cylinder with a radius of 45 mm exposed to a reported total enthalpy of 22.4 MJ/kg. The experimental setup is numerically replicated by imposing the inflow conditions given in Table 6 on the left boundary. The freestream Reynolds number based on the cylinder diameter is $Re_\infty = 18778$. Symmetry is imposed along the stagnation line, and the outer boundaries are set as non-reflecting outlets. The reaction mechanism employed for the 5-species air model is taken from Park [54,55]. As remarked by Knight et al. [3], there appears to be a large variation in the results from different solvers, especially regarding the treatment of the surface. To study this sensitivity, three different surface conditions are tested in the following sections: two inert cases with adiabatic and isothermal conditions, and a third case with a fully catalytic isothermal wall.

In the following assessment of IB methods, we compare the cut-cell (CC) method of INCA with the ghost-point (GP) method of CHESS, and

Table 6
Freestream conditions for the 2-D cylinder case.

M_∞	u_∞ [m/s]	T_∞ [K]	p_∞ [Pa]	ρ_∞ [kg/m^3]	$y(N_2)$	$y(O_2)$	y(NO)	y(N)	y(O)
8.98	5956	901	476	1.547×10^{-3}	0.7543	0.00713	0.01026	6.5×10^{-7}	0.2283

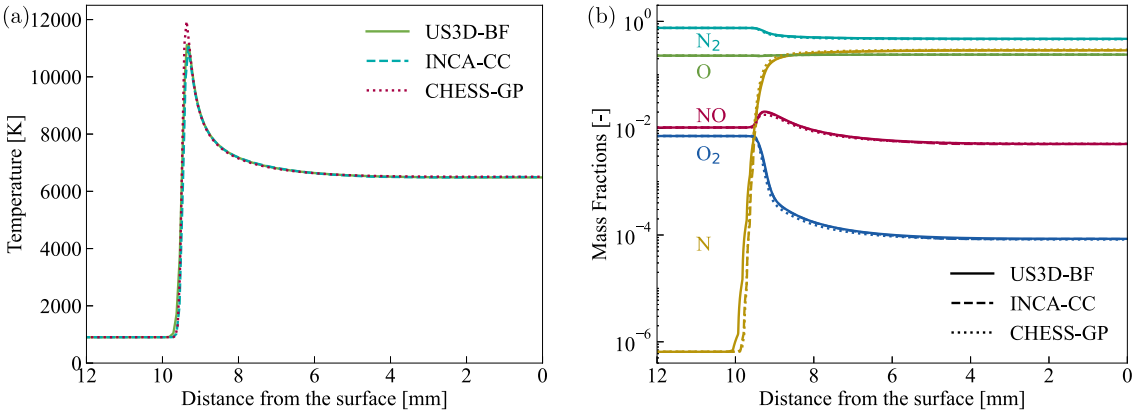

Fig. 7. Comparison of (a) temperature and (b) mass fractions along the stagnation line for the inert adiabatic 2-D cylinder case.

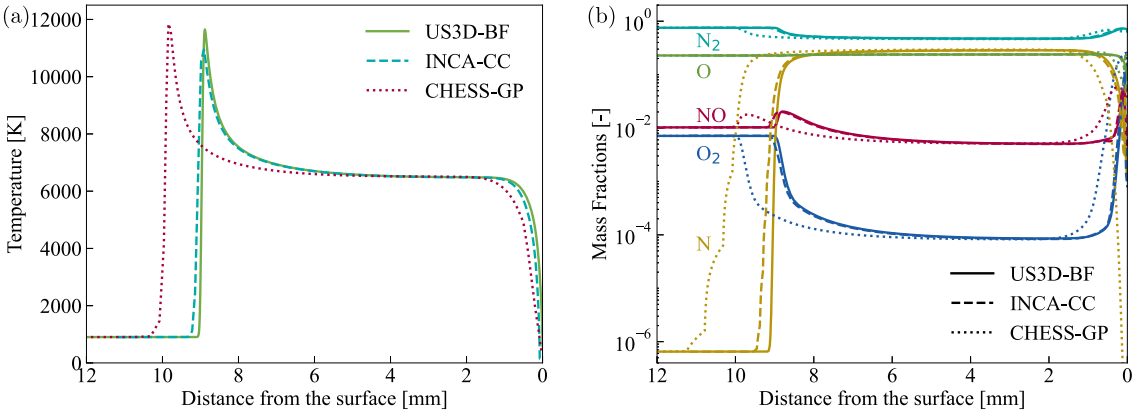

Fig. 8. Comparison of (a) temperature and (b) mass fractions along the stagnation line for the inert isothermal 2-D cylinder case by Knight et al. [3].

results obtained with the body-fitted (BF) method of US3D are taken as reference. These methods are indicated after a short dash next to the solver names for clarity as US3D-BF, INCA-CC, and CHESS-GP.

4.5.1. Inert adiabatic wall

The temperature and species mass fractions along the stagnation line are presented for the adiabatic case in Fig. 7. Shock stand-off distance and the dissociation of molecular nitrogen and oxygen in the shock layer are predicted in very good agreement by all methods. The fundamental differences in the implementation of the adiabatic wall boundary condition in BF and IB solvers have no noticeable effect on the results. This is in line with the expectation that numerical truncation and conservation errors are small in the absence of strong gradients.

4.5.2. Inert isothermal wall

For the same inflow conditions, an isothermal wall boundary condition with a wall temperature of 300 K is imposed on the cylinder surface, in accordance with the specifications by Knight et al. [3]. The numerical predictions for the stagnation line temperature and mass fraction distributions are plotted in Fig. 8. Results obtained with the US3D-BF and INCA-CC methods match almost exactly, including the steep temperature and species variations in the boundary layer. Results obtained with the CHESS-GP method, on the other hand, show a significant difference in the shock stand-off distance. This could

Table 7
Grid resolution and stagnation point details for the inert isothermal 2-D cylinder case, where Δh_w is the effective wall-normal cell size at the wall, p_0 is the stagnation point pressure, and $q_{w,0}$ is the stagnation point wall heat flux.

Solver & Grid resolution	Δh_w [μm]	p_0 [kPa]	$q_{w,0}$ [MW/m^2]
Experiment [3]	N/A	52.26 ± 3.034	7.402 ± 0.220
Nompelis [3]	7.0[a]	52.40	5.971
US3D-BF (coarse)	0.44	54.38	8.422
US3D-BF (medium-coarse)	0.22	53.29	7.576
US3D-BF (medium-fine)	0.1	53.05	7.345
US3D-BF (fine)	0.05	52.95	7.308
INCA-CC (coarse)	2.5	51.57	6.684
INCA-CC (medium-coarse)	1.25	51.57	7.028
INCA-CC (medium-fine)	0.625	51.58	7.144
INCA-CC (fine)	0.3125	51.58	7.189
CHESS-GP [16,17]	3.0	52.83	0.167

[a] Personal communication with Ioannis Nompelis.

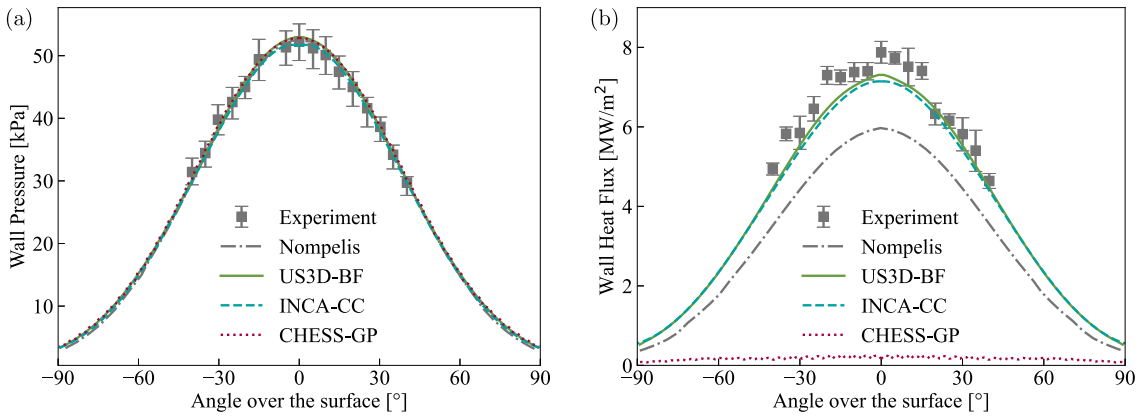

Fig. 9. Comparison of surface (a) pressures and (b) heat fluxes for the inert isothermal 2-D cylinder case by Knight et al. [3].

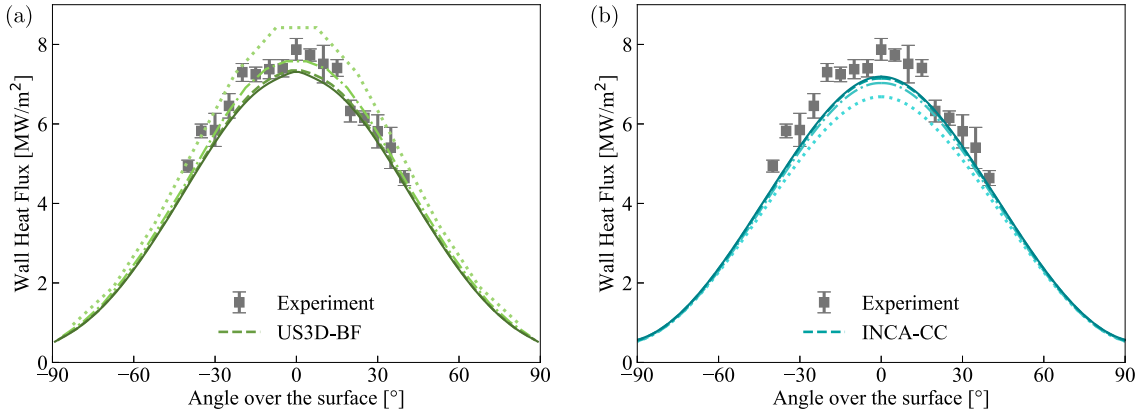

Fig. 10. Grid convergence studies with the (a) US3D-BF and (b) INCA-CC methods considering surface heat fluxes for the inert isothermal 2-D cylinder case by Knight et al. [3]. Four levels of refinement are shown: coarse (·····), medium-coarse (— · — · —), medium-fine (— — — —), and fine (————).

be attributed to the non-conservative formulation of the ghost-cell IB methodology. Mass conservation errors could manifest as an non-physical blowing from the surface. Consequently, the shock stand-off distance is increased and the whole flow field is modified. The adiabatic case is less affected by these conservation errors because it has much smaller temperature and density gradients near the wall. The INCA-CC method handles large temperature and density gradients at isothermal walls much better, because it uses a strictly conservative IB method.

In Fig. 9, surface pressure and heat flux distributions are compared with the experimental measurements from Knight et al. [3] and also with the numerical simulations of Nompelis from the same publication. All methods accurately predict the pressure distribution. Heat flux predictions of the US3D-BF and INCA-CC methods are in very good agreement. They match the experimental measurements better than the numerical simulations of Nompelis. Slight differences in heat fluxes are expected to be due to the differences in grid resolutions at the surface. Grid convergence studies have been carried out with both the US3D-BF and INCA-CC methods as summarized in Table 7 and showcased for the variation in heat fluxes in Fig. 10. Four levels of resolution are considered with the minimum cell size at the surface approximately halving with each step. An interesting observation is that the INCA-CC method under-predicts the heat flux on coarse meshes, as intuitively expected, whereas the US3D-BF method over-predicts the heat flux on coarse meshes. This difference in the convergence trend is a sign of complex interactions between transport and chemistry. For both solvers, results obtained on the medium-fine resolution mesh are considered grid converged, as they are essentially identical to the results obtained on the fine meshes. The structure of both medium-fine grids is shown in Fig. 11. For these grids, the smallest cell size near the wall is 1.0×10^{-7} m for the US3D-BF method and 6.25×10^{-7} m for the INCA-CC method, and the total number of cells are 38216 and 2875600, respectively.

For this case, the CHESS-GP method is not able to predict the heat flux correctly. A similar underprediction has also been reported in literature for another ghost-cell IB-AMR solver by Brahmachary et al. [12], where the issue has been linked to the reconstruction of temperature by linear interpolation. However, the cut-cell IB method also resorts to second-order reconstruction schemes and can predict the heat flux correctly. Therefore, we attribute the observed deficiencies to conservation errors incurred through the ghost-cell IB method. This hypothesis is further discussed in Section 5, where also results obtained with the independently developed INCA-GP method are presented.

4.5.3. Catalytic isothermal wall

Exothermic catalytic reactions enhance the surface heat flux through a diffusive heat flux contribution. A fully catalytic wall ($\gamma = 1.0$) at the same temperature of 300 K is considered, as Karl et al. [58] state that this boundary condition is closest to what they have assumed for the experiments. It is, however, reasonable to assume that fully catalytic conditions were only achieved for a short duration at the beginning of the experiment. The fully catalytic boundary condition

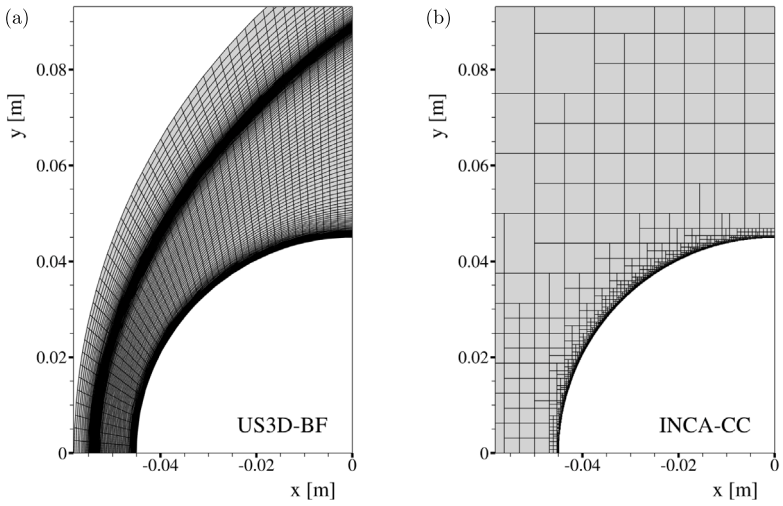

Fig. 11. Computational grids used by (a) US3D-BF and (b) INCA-CC (AMR block structure is shown) for the catalytic isothermal 2-D cylinder case.

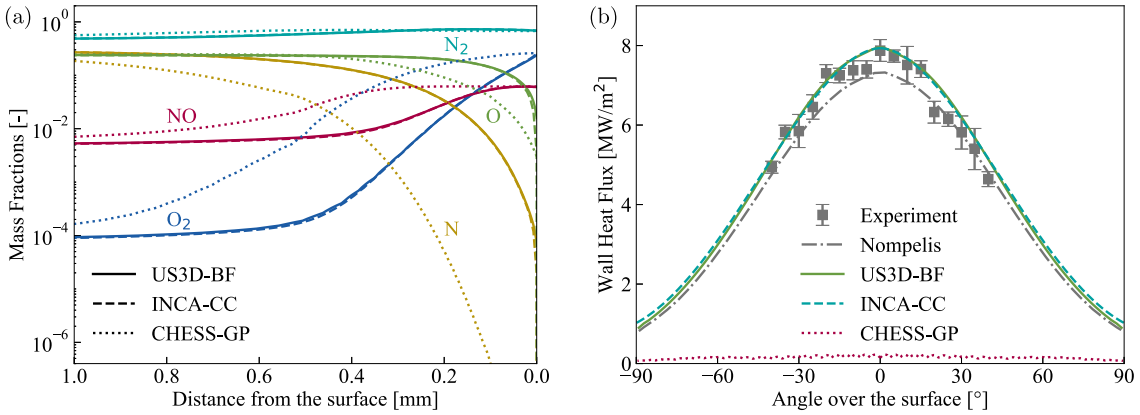

Fig. 12. Comparison of (a) mass fractions along the stagnation line and (b) heat fluxes over the surface for the catalytic isothermal 2-D cylinder case by Knight et al. [3].

imposes the recombination of all atoms impinging on the surface, while still respecting the physical limits set by species diffusion.

The species mass fractions along the stagnation line and the total surface heat flux distributions are shown in Fig. 12. Predictions of the US3D-BF and INCA-CC methods are in excellent agreement, both in terms of species concentrations and surface heat fluxes. Because the cold wall itself already promotes recombination reactions in the boundary layer, accounting for catalysis leads only to a minor increase in the heat fluxes, which remain within the experimental uncertainties. It is therefore difficult to draw conclusions on the effective value of the recombination coefficient in the experiment.

Another interesting observation could be made by comparing the level of agreement between the heat fluxes obtained with the US3D-BF and INCA-CC methods for the inert wall shown in Fig. 9 and for the fully catalytic wall shown in Fig. 12. Taking the US3D-BF method as reference, it is seen that at the stagnation point, results of the INCA-CC method with the inert wall are 2.7% lower, while with the fully catalytic wall the difference is only 0.2%. It can be argued that this better agreement is mostly associated with the dominant nature of the catalytic boundary condition. Our previous comments regarding the differences of the CHESS-GP results for the inert isothermal case apply here as well.

To complete the analysis, contour plots are presented for Mach numbers in Fig. 13, for temperatures in Fig. 14, and for atomic nitrogen concentrations in Fig. 15. These contour plots further confirm the preceding quantitative discussions by once again reflecting the excellent agreement between the US3D-BF and INCA-CC methods. From the trace of the sonic line, to the peak shock temperatures, and to the extent of the species boundary layer marked by nitrogen accumulation, the results are in perfect agreement.

4.6. 2-D ablator

A subsonic plasma wind tunnel experiment conducted at the von Karman Institute for Fluid Dynamics (VKI) by Helber et al. [53] is considered to assess the IB methods for GSI with ablative boundary conditions. The experiment exposes a graphite sample with a hemispherical nose of radius 25 mm and a cylindrical downstream extension of 250 mm to nitrogen plasma.

The sample undergoes ablation through nitridation reactions

$$C_{(solid)} + N \rightarrow CN\,, \tag{12}$$

which we model according to Eqs. (8)–(11) with the nitridation efficiency coefficient

$$\gamma = 7.91 \cdot 10^{-2} \exp\left(-\frac{5663}{T_{wall}}\right)\,. \tag{13}$$

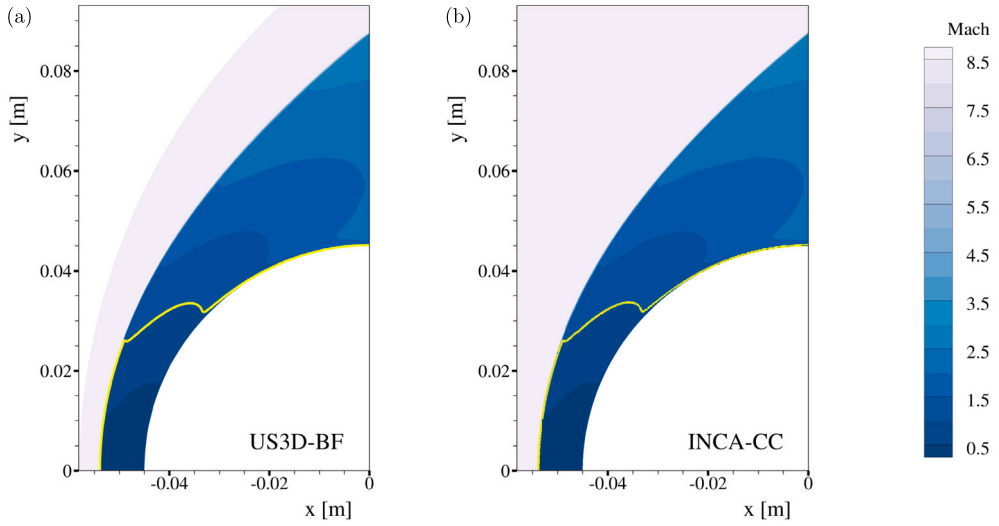

Fig. 13. Mach number contours for the catalytic isothermal 2-D cylinder case obtained with the (a) US3D-BF and (b) INCA-CC methods. The sonic line is shown in yellow.

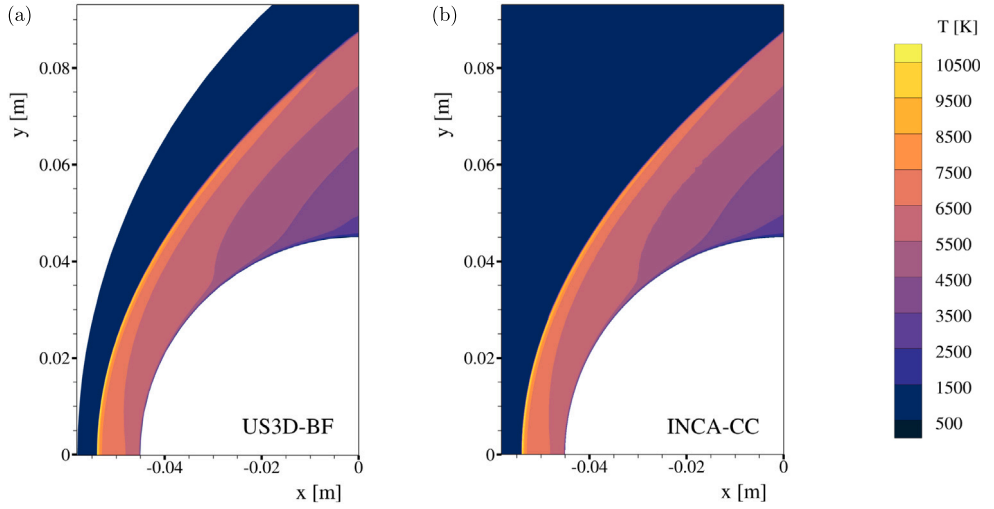

Fig. 14. Temperature contours for the catalytic isothermal 2-D cylinder case obtained with the (a) US3D-BF and (b) INCA-CC methods.

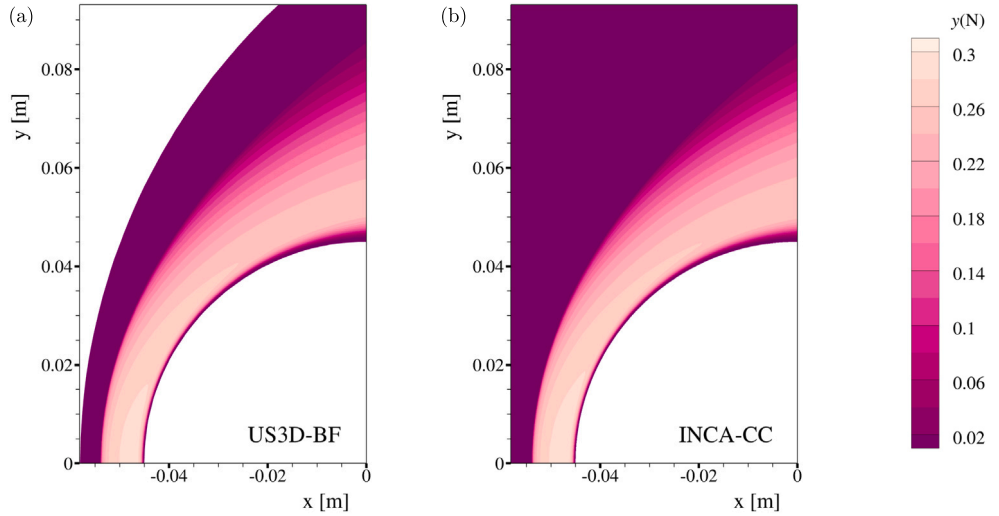

Fig. 15. Atomic nitrogen mass fraction contours for the catalytic isothermal 2-D cylinder case obtained with the (a) US3D-BF and (b) INCA-CC methods.

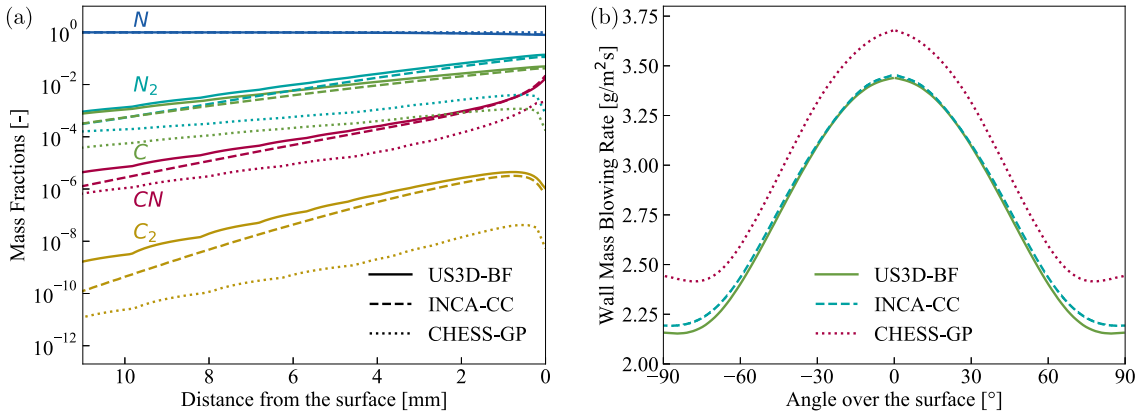

Fig. 16. Comparison of (a) mass fractions along the stagnation line and (b) mass blowing rates over the surface for the 2-D ablator case.

Table 8
Freestream conditions for the 2-D ablator case.

u_∞ [m/s]	T_∞ [K]	T_{wall} [K]	p_∞ [Pa]	$y(N_2)$	$y(N)$
1570	10 280	2407	1500	9.77659e−05	0.9999022341

The nitridation efficiency was calibrated based on these particular experiments [53]. The simulations discussed in the following include mass blowing due to ablation over the sample, but do not account for the very slow shape change of the sample.

First, we reproduced the experiment numerically using the US3D-BF method. For these simulations, a 9-species nitrogen-carbon mixture was considered, including free electrons and ionized species. These simulations yielded a stagnation point mass blowing rate of 3.41 g/m^2s, which is within the experimental uncertainty range set by 2.8864 ∓ 0.965 g/m^2s. The ablation model based on Eq. (13) is thus validated.

Having confidence in the ablation model and its implementation in the US3D-BF method, the experimental test case is simplified to a 2-D geometry without ionized species to reduce the computational cost and to avoid straying too far from the objective of evaluating immersed boundary methods for an ablative boundary condition. Freestream conditions of this 2-D case are given in Table 8. A 6-species mixture of $[N_2, N, CN, C_3, C_2, C]$ is considered with chemical mechanisms from Olynick et al. [59]. For all methods, the grid resolution at the wall is 1×10^{-5} m in the wall-normal direction, which leads to 35838 cells for the US3D-BF method and 231300 cells for the INCA-CC method. Grid structures are presented in Fig. 17.

The mass fractions along the stagnation line and the mass blowing rates over the wall are shown in Fig. 16. Mass fractions for C_3 are not seen as they are almost zero. Predictions of the US3D-BF and INCA-CC methods agree well with each other. Overall, the production of CN at the wall and the dissociation of it through gas-phase reactions to form atomic nitrogen are well captured. Mass blowing rates from the US3D-BF and INCA-CC methods are also in very good agreement. Results obtained with the CHESS-GP method show noticeable discrepancies for the mass fractions along the stagnation line and for the surface mass blowing rates. Despite the apparent quantitative mismatch, also the CHESS-GP method captures the profiles qualitatively well in the absence of strong gradients near the wall.

Temperature and atomic nitrogen contours for the US3D-BF and INCA-CC methods are shown in Figs. 18 and 19. Results of both methods agree very well on the thermal gradient over the surface and on the recombination of nitrogen as temperature drops.

5. On the importance of conservative boundary conditions

In the previous section, we have demonstrated that INCA with its cut-cell IB method on block-Cartesian AMR meshes performs on par with the reference solver US3D employing body-fitted meshes. The ghost-cell IB method of CHESS [16] is in a good agreement with the other methods for the first four verification studies and for the cylinder with adiabatic walls exposed to high-enthalpy hypersonic flow conditions; however, it cannot predict the heat flux at strongly cooled walls. We have attributed these inaccuracies to mass conservation errors as this is the most striking difference between ghost-cell methods and the strictly conservative cut-cell approach. However, the three solvers clearly differ also in several other aspects, such as the numerical schemes used for advection and diffusion driving forces. Hence, it remains uncertain whether the observed shortcomings are inherent to the ghost-cell method itself or specific to a particular implementation. To further corroborate the superiority of a conservative cut-cell (or cut-element) IB methodology, we have also applied the ghost-cell method of INCA for selected cases. By switching off the special flux treatment in cut-cells employed in the preceding sections, a standard ghost-cell method is obtained that only relies on the extrapolated fluid solutions near the boundary as described in Section 3. Without the cut-cell procedure, mass, momentum, and energy conservation are not exactly satisfied. The resulting INCA-GP method has nominally the same order of convergence as INCA's conservative cut-element method, INCA-CC.

A comparison of INCA-GP and INCA-CC predictions is presented for the two most challenging benchmark cases in Fig. 20. It can be seen that, regardless of the various differences between the INCA-GP and CHESS-GP methods, both ghost-cell methods are unsuccessful in predicting the surface heat fluxes and the mass blowing rates. For the 2-D cylinder case with an isothermal wall, the heat flux prediction of the INCA-GP method is closer in magnitude to the INCA-CC results and to the US3D-BF reference data than to the results obtained with the CHESS-GP method; however, both ghost-cell methods give clearly wrong results. The grid sensitivity of the INCA-GP results is presented in Fig. 22a for the same resolutions as in Fig. 10 for the INCA-CC method. Results of the INCA-GP method non-monotonically approach closer to the experimental measurements with finer grid resolution and on the finest grid quantitatively match the reference data away

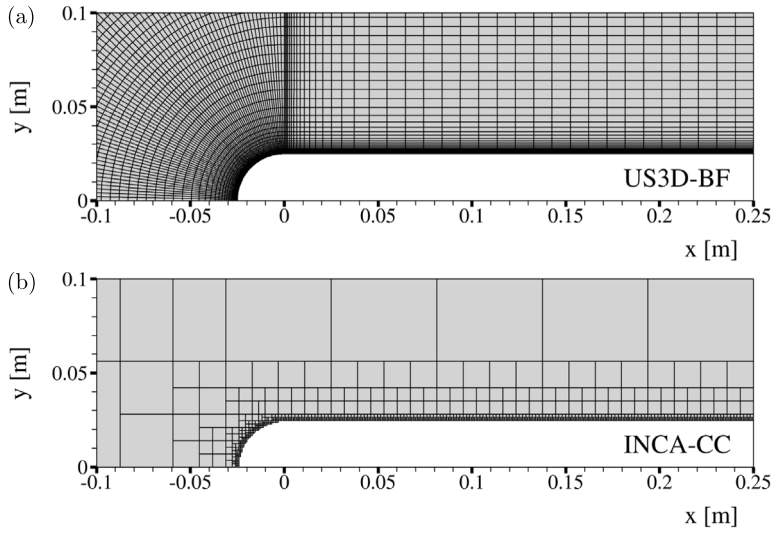

Fig. 17. Computational grids used by (a) US3D-BF and (b) INCA-CC (AMR block structure is shown) for the 2-D ablator case.

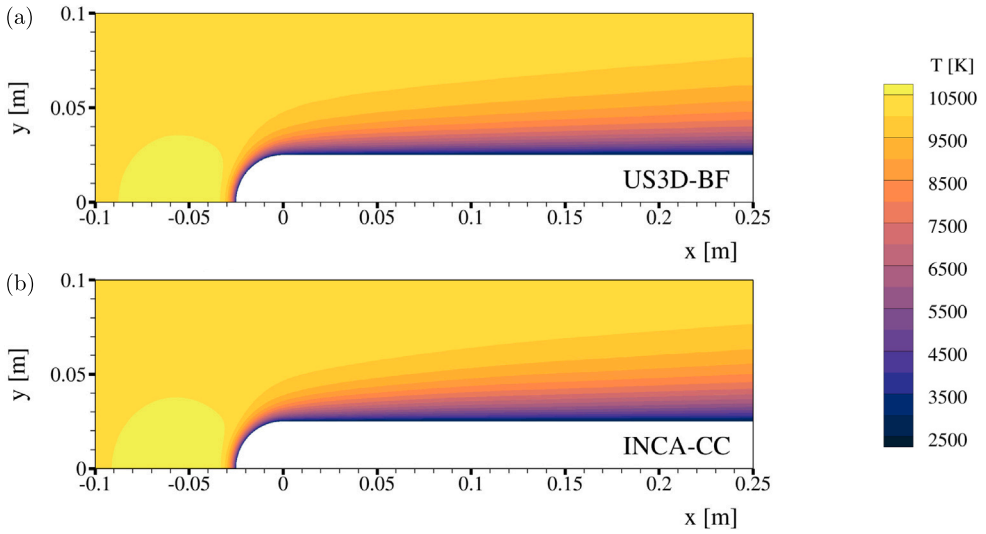

Fig. 18. Comparison of the temperature contours for the 2-D ablator case obtained with the (a) US3D-BF and (b) INCA-CC methods.

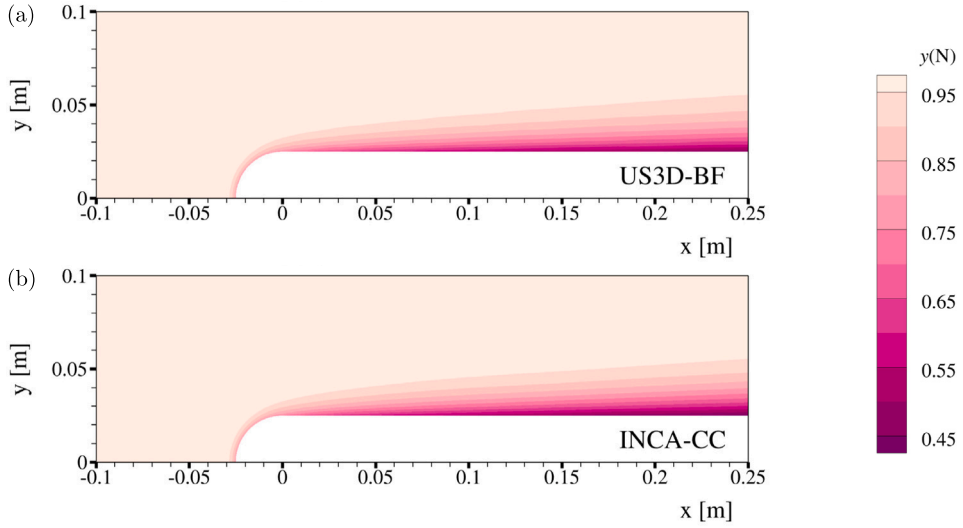

Fig. 19. Comparison of the atomic nitrogen mass fraction contours for the 2-D ablator case obtained with the (a) US3D-BF and (b) INCA-CC methods.

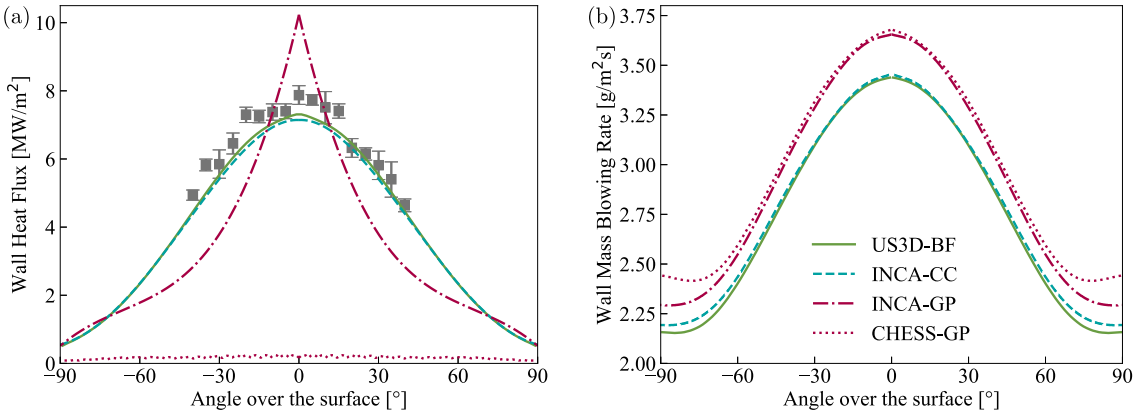

Fig. 20. Comparison of (a) heat fluxes over the surface for the isothermal 2-D cylinder case by Knight et al. [3] and (b) mass blowing rates for the 2-D ablator case.

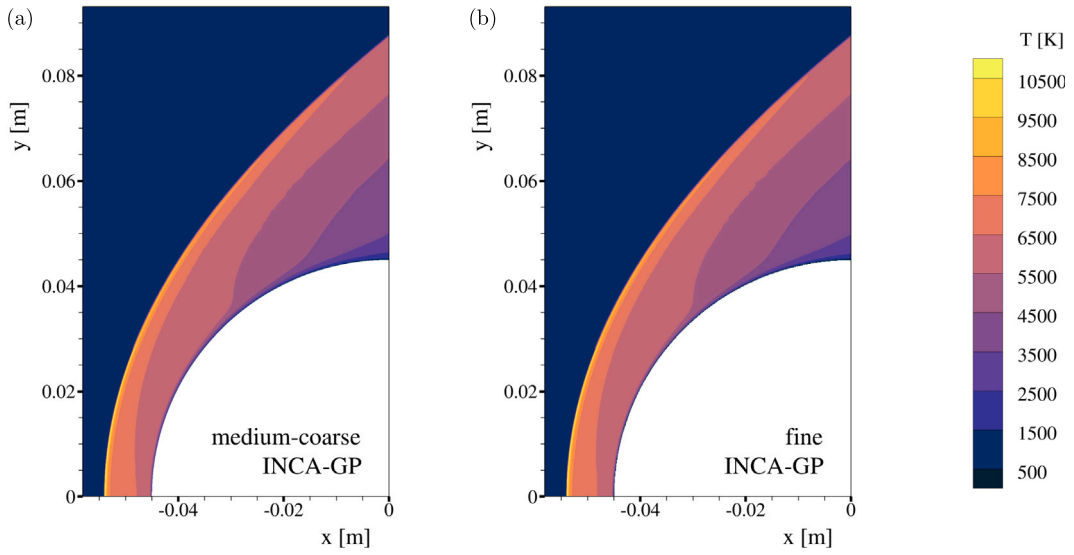

Fig. 21. Temperature contours for the isothermal 2-D cylinder case obtained with the ghost-cell method of INCA on (a) medium-coarse and (b) fine resolution grids.

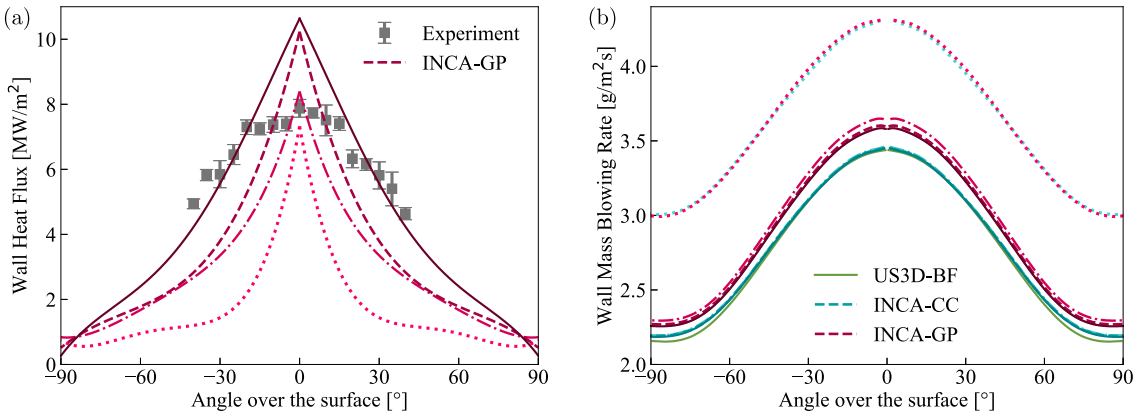

Fig. 22. Grid convergence studies (a) with the INCA-GP method for the isothermal 2-D cylinder case (compare with INCA-CC and US3D-BF results shown in Fig. 10) and (b) with the INCA-CC and INCA-GP methods for the 2-D ablator case. Legend: coarse (·····), medium-coarse (— · — · —), medium-fine (— — — —), and fine (————) grid.

from the stagnation point. However, the shape of the profile still does not match the results of the INCA-CC and US3D-BF methods. Errors attributed to the lack of conservation in the ghost-cell methods are larger closer to the stagnation point, where gradients are higher, leading to overpredictions as seen from the results. Temperature contours for the medium-coarse and the finest grids are shown in Fig. 21. These contours are visually indistinguishable from the contours presented in Fig. 14 for the INCA-CC method. This further confirms that the errors in heat flux originate at the surface level and have a negligible impact on the flow field.

For the ablative case, the INCA-GP method yields a surprisingly similar prediction as the CHESS-GP method, as shown in Fig. 20b for the medium-fine grid. INCA-CC and INCA-GP grid convergence studies are presented for this case in Fig. 22b. It can be seen that results with both methods match on the coarsest grid, where the surface quantities are only roughly estimated. The cut-cell method demonstrates a swift convergence to the US3D-BF reference results, making the medium-coarse and finer resolutions nearly indistinguishable in the plot. In contrast, the ghost-cell method exhibits a slower grid convergence and the converged fine-grid solution retains a noticeable offset from the reference data.

Comparable inaccuracies are evident in two independently developed ghost-cell IB methods, CHESS-GP and INCA-GP. The only difference between the INCA-GP method and INCA's cut-cell method, which demonstrated excellent agreement with the reference data, is the conservative flux treatment. This further reinforces our assessment that conservation errors intrinsic to ghost-cell IB methods are the root cause of the large errors observed at cold walls. It is expected that these conservation errors remain small unless gradients of the conservative variables are very large. This explains why errors manifest at cold walls and not at adiabatic walls.

6. Conclusion

We have evaluated the accuracy of immersed boundary methods for atmospheric entry conditions, including the influence of chemical nonequilibrium and gas–surface interactions. The eight benchmark cases assess the accurate modelling of gas chemistry, mass diffusion, surface catalysis, and surface mass blowing due to ablation.

Computational results obtained with the cut-element IB method in the AMR solver INCA are in an almost perfect agreement with the reference data for all considered cases, and as accurate as the results obtained with US3D on body-fitted meshes. Particularly for surface heat flux and mass blowing rate predictions, the benefit of an IB method that strictly conserves mass, momentum, and energy, such as the cut-element method in INCA, is clearly demonstrated in this study. After comparing this method with two non-conservative IB methods implemented in INCA and in an independently developed solver, we saliently remark that numerical anomalies causing mispredictions of sensitive surface quantities can occur when using non-conservative IB formulations.

CFD solvers that provide automatic mesh generation and adaptation to represent detailed and moving geometries with IB methods have many promising advantages; however, the accuracy of the numerical schemes used for computing surface quantities must be analyzed rigorously before they can be used for predictive simulations. The selection of a set of well-defined test cases by mutual collaboration between research groups is crucial in converging to a robust consensus on the prediction of these surface states. To that end, this paper establishes a comprehensive set of fundamental benchmark cases with reacting surfaces, which can be used for the verification and validation of hypersonic flow solvers. We hope the community will welcome this benchmark suite for assessing the accuracy of immersed boundary methods for atmospheric entry applications.

CRediT authorship contribution statement

Ata Onur Başkaya: Conceptualization, Methodology, Formal analysis, Writing. **Michele Capriati:** Methodology, Formal analysis. **Alessandro Turchi:** Supervision. **Thierry Magin:** Supervision. **Stefan Hickel:** Conceptualization, Methodology, Writing, Supervision, Project administration.

Declaration of competing interest

The authors declare that they have no known competing financial interests or personal relationships that could have appeared to influence the work reported in this paper.

Data availability

Data will be made available on request.

Acknowledgements

We extend our sincere appreciation to Prof. Giuseppe Pascazio, Dr. Francesco Bonelli, and Dr. Davide Ninni from Politecnico di Bari for their valuable collaboration, insightful discussions regarding methods and results, and their comments on the manuscript. From TU Delft, we thank Prof. Georg Eitelberg for his insights concerning the experiments carried out at DLR and Dr. Ferdinand Schrijer for his critical feedback on the manuscript. We acknowledge the Delft High Performance Computing Center (DHPC) for providing access to DelftBlue, the SURF Cooperative (www.surf.nl) for their services, and the Dutch Research Council (NWO) for providing access to Snellius.

Appendix

Analytical solution of the 1-D catalytic diffusion problem

Following the derivation proposed by Bariselli [60], substituting Fick's law into the molar continuity equation, and solving for the zero-advection, constant temperature, steady-state solution one obtains

$$\nabla \cdot \left(n \frac{M_{\mathrm{N}}}{\overline{M}} D_{\mathrm{N}_2,\mathrm{N}} \nabla(x_{\mathrm{N}_2}) \right) = 0 \,, \tag{A.1}$$

with n as the number density. For the current binary mixture $M_{N_2} = 2M_N$ and $\overline{M} = \sum_i x_i M_i$, which in 1-D leads to

$$\frac{d}{d\eta} \left(\frac{1}{x_{\mathrm{N}_2} + 1} \left(\frac{d}{d\eta} x_{\mathrm{N}_2} \right) \right) = 0 \,, \tag{A.2}$$

with η as the spatial coordinate. Solving for x_{N_2} yields

$$x_{\mathrm{N}_2} = \frac{e^{C_1 M_{\mathrm{N}} \eta} e^{C_2 M_{\mathrm{N}}}}{M_{\mathrm{N}}} \,, \tag{A.3}$$

with C_1 and C_2 as integration constants to be found through the boundary conditions. Firstly, by knowing that $\left(X_{\mathrm{N}_2}\right)_{\eta=0} = 0$ at the free-stream reservoir

$$C_2 = \frac{\ln M_{\mathrm{N}}}{M_{\mathrm{N}}} \,. \tag{A.4}$$

Secondly, by equating the diffusion flux to the chemical production rate at the wall, $(J_{\mathrm{N}_2} = \dot{\omega}_{\mathrm{N}_2})_{\eta=L}$, which gives

$$\left(\frac{C_1 M_{\mathrm{N}}}{2 - e^{C_1 L M_{\mathrm{N}}}} = \frac{\gamma_{\mathrm{N}}}{2 D_{\mathrm{N}_2\mathrm{N}}} \sqrt{\frac{k_B T}{2\pi m_{\mathrm{N}}}} \right)_{\eta=L} \,, \tag{A.5}$$

where k_B is the Boltzmann constant. The last expression can be solved iteratively through the Newton–Raphson method. The solution describes the species distribution as a function of spatial variable η.

References

[1] Gu S, Olivier H. Capabilities and limitations of existing hypersonic facilities. Prog Aerosp Sci 2020;113:100607.
[2] Wright MJ, White T, Mangini N. Data parallel line relaxation (DPLR) code user manual: Acadia version 4.01. 1. National Aeronautics and Space Administration, Ames Research Center; 2009.
[3] Knight D, Longo J, Drikakis D, Gaitonde D, Lani A, Nompelis I, et al. Assessment of CFD capability for prediction of hypersonic shock interactions. Prog Aerosp Sci 2012;48:8–26.
[4] Knight D, Chazot O, Austin J, Badr MA, Candler G, Celik B, et al. Assessment of predictive capabilities for aerodynamic heating in hypersonic flow. Prog Aerosp Sci 2017;90:39–53.
[5] Candler G, Mavriplis D, Trevino L. Current status and future prospects for the numerical simulation of hypersonic flows. AIAA paper 2009-153; 2009.

[6] Candler GV, Johnson HB, Nompelis I, Gidzak VM, Subbareddy PK, Barnhardt M. Development of the US3D code for advanced compressible and reacting flow simulations. AIAA paper 2015-1893; 2015.

[7] Scalabrin L, Boyd I. Development of an unstructured Navier-Stokes solver for hypersonic nonequilibrium aerothermodynamics. AIAA paper 2005-5203; 2005.

[8] Arslanbekov R, Kolobov V, Frolova A. Analysis of compressible viscous flow solvers with adaptive Cartesian mesh. AIAA paper 2011-3381; 2011.

[9] Sekhar SK, Ruffin SM. Predictions of convective heat transfer rates using a Cartesian grid solver for hypersonic flows. AIAA paper 2013-2645; 2013.

[10] Atkins C, Deiterding R. Towards a strand-Cartesian solver for modelling hypersonic flows in thermochemical non-equilibrium. AIAA paper 2020-2404; 2020.

[11] McQuaid JA, Zibitsker AL, Saikia B, Martin A, Brehm C. An immersed boundary method for hypersonic viscous flows. AIAA paper 2021-0926; 2021.

[12] Brahmachary S, Natarajan G, Kulkarni V, Sahoo N, Ashok V, Kumar V. Role of solution reconstruction in hypersonic viscous computations using a sharp interface immersed boundary method. Phys Rev E 2021;103(4):043302.

[13] Mittal R, Iaccarino G. Immersed boundary methods. Annu Rev Fluid Mech 2005;37:239–61.

[14] Hickel S, Egerer CP, Larsson J. Subgrid-scale modeling for implicit large eddy simulation of compressible flows and shock-turbulence interaction. Phys Fluids 2014;26(10):106101.

[15] Müller H, Niedermeier CA, Matheis J, Pfitzner M, Hickel S. Large-eddy simulation of nitrogen injection at trans-and supercritical conditions. Phys Fluids 2016;28(1):015102.

[16] Başkaya AO, Capriati M, Ninni D, Bonelli F, Pascazio G, Turchi A, et al. Verification and validation of immersed boundary solvers for hypersonic flows with gas-surface interactions. AIAA paper 2022-3276; 2022.

[17] Ninni D. Development of a multi-GPU solver for atmospheric entry flows with gas-surface interactions [Ph.D. thesis], Politecnico di Bari; 2022.

[18] Scoggins JB, Leroy V, Bellas-Chatzigeorgis G, Dias B, Magin TE. Mutation++: Multicomponent thermodynamic and transport properties for ionized gases in C++. SoftwareX 2020;12:100575.

[19] Park C. Nonequilibrium hypersonic aerothermodynamics. Wiley New York; 1989.

[20] Sutton K, Gnoffo P. Multi-component diffusion with application to computational aerothermodynamics. AIAA paper 1998-2575; 1998.

[21] Wilke C. A viscosity equation for gas mixtures. J Chem Phys 1950;18(4):517–9.

[22] Mason E, Saxena S. Approximate formula for the thermal conductivity of gas mixtures. Phys Fluids 1958;1(5):361–9.

[23] Sarma G. Physico–chemical modelling in hypersonic flow simulation. Prog Aerosp Sci 2000;36(3–4):281–349.

[24] Park C. The limits of two-temperature kinetic model in air. AIAA paper 2010-911; 2010.

[25] Magin TE, Panesi M, Bourdon A, Jaffe RL, Schwenke DW. Coarse-grain model for internal energy excitation and dissociation of molecular nitrogen. Chem Phys 2012;398:90–5.

[26] Alkandry H, Boyd I, Martin A. Comparison of models for mixture transport properties for numerical simulations of ablative heat-shields. AIAA paper 2013-303; 2013.

[27] Miró Miró F, Beyak ES, Pinna F, Reed HL. High-enthalpy models for boundary-layer stability and transition. Phys Fluids 2019;31(4):044101.

[28] Hollis BR, Prabhu DK. Assessment of laminar, convective aeroheating prediction uncertainties for Mars-entry vehicles. J Spacecr Rockets 2013;50(1):56–68.

[29] Candler G. Nonequilibrium processes in hypervelocity flows: an analysis of carbon ablation models. AIAA paper 2012-724; 2012.

[30] McBride BJ, Zehe MJ, Gordon S. NASA Glenn coefficients for calculating thermodynamic properties of individual species. Technical report NASA/TP—2002-211556, Glenn Research Center; 2002.

[31] Chapman S, Cowling TG. The mathematical theory of non-uniform gases: An account of the kinetic theory of viscosity, thermal conduction and diffusion in gases. Cambridge University Press; 1990.

[32] Bellas Chatzigeorgis G, Turchi A, Viladegut A, Chazot O, Barbante PF, Magin T. Development of catalytic and ablative gas-surface interaction models for the simulation of reacting gas mixtures. AIAA paper 2017-4499; 2017.

[33] Barbante PF. Accurate and efficient modelling of high temperature nonequilibrium air flows [Ph.D. thesis], Université libre de Bruxelles; 2001.

[34] Mittal R, Dong H, Bozkurttas M, Najjar F, Vargas A, Von Loebbecke A. A versatile sharp interface immersed boundary method for incompressible flows with complex boundaries. J Comput Phys 2008;227(10):4825–52.

[35] de Tullio MD, De Palma P, Iaccarino G, Pascazio G, Napolitano M. An immersed boundary method for compressible flows using local grid refinement. J Comput Phys 2007;225(2):2098–117.

[36] Ye T, Mittal R, Udaykumar H, Shyy W. An accurate Cartesian grid method for viscous incompressible flows with complex immersed boundaries. J Comput Phys 1999;156(2):209–40.

[37] Udaykumar H, Mittal R, Rampunggoon P, Khanna A. A sharp interface Cartesian grid method for simulating flows with complex moving boundaries. J Comput Phys 2001;174(1):345–80.

[38] Meyer M, Devesa A, Hickel S, Hu X, Adams NA. A conservative immersed interface method for large-eddy simulation of incompressible flows. J Comput Phys 2010;229(18):6300–17.

[39] Steger JL, Warming R. Flux vector splitting of the inviscid gasdynamic equations with application to finite-difference methods. J Comput Phys 1981;40(2):263–93.

[40] Van Leer B. Towards the ultimate conservative difference scheme. V. A second-order sequel to Godunov's method. J Comput Phys 1979;32(1):101–36.

[41] Wright MJ, Candler GV, Bose D. Data-parallel line relaxation method for the Navier-Stokes equations. AIAA J 1998;36(9):1603–9.

[42] Capriati M, Prata KS, Schwartzentruber TE, Candler GV, Magin TE. Development of a nitridation gas-surface boundary condition for high-fidelity hypersonic simulations. In: 14th WCCM-ECCOMAS congress 2020, vol. 600. 2021.

[43] Jiang G-S, Shu C-W. Efficient implementation of weighted ENO schemes. J Comput Phys 1996;126(1):202–28.

[44] Toro EF. Riemann solvers and numerical methods for fluid dynamics: A practical introduction. Berlin: Springer-Verlag; 2013.

[45] Gottlieb S, Shu C-W. Total variation diminishing Runge-Kutta schemes. Math Comput 1998;67(221):73–85.

[46] Strang G. On the construction and comparison of difference schemes. SIAM J Numer Anal 1968;5(3):506–17.

[47] Brown PN, Byrne GD, Hindmarsh AC. VODE: A variable-coefficient ODE solver. SIAM J Sci Stat Comput 1989;10(5):1038–51.

[48] Örley F, Pasquariello V, Hickel S, Adams NA. Cut-element based immersed boundary method for moving geometries in compressible liquid flows with cavitation. J Comput Phys 2015;283:1–22.

[49] Pasquariello V, Hammerl G, Örley F, Hickel S, Danowski C, Popp A, et al. A cut-cell finite volume–finite element coupling approach for fluid–structure interaction in compressible flow. J Comput Phys 2016;307:670–95.

[50] Ingram DM, Causon DM, Mingham CG. Developments in Cartesian cut cell methods. Math Comput Simulation 2003;61(3–6):561–72.

[51] Schneiders L, Günther C, Meinke M, Schröder W. An efficient conservative cut-cell method for rigid bodies interacting with viscous compressible flows. J Comput Phys 2016;311:62–86.

[52] Baskaya AO, Hickel S. A conservative cut-cell immersed boundary method for accurate simulation of hypersonic flows with gas-surface interactions. In: 57th 3AF international conference on applied aerodynamics. 2023.

[53] Helber B, Turchi A, Magin TE. Determination of active nitridation reaction efficiency of graphite in inductively coupled plasma flows. Carbon 2017;125:582–94.

[54] Park C. Review of chemical-kinetic problems of future NASA missions. I-Earth entries. J Thermophys Heat Transfer 1993;7(3):385–98.

[55] Park C, Jaffe RL, Partridge H. Chemical-kinetic parameters of hyperbolic earth entry. J Thermophys Heat Transfer 2001;15(1):76–90.

[56] Grossman B, Cinnella P. Flux-split algorithms for flows with non-equilibrium chemistry and vibrational relaxation. J Comput Phys 1990;88(1):131–68.

[57] Park C. On convergence of computation of chemically reacting flows. AIAA paper 1985-247; 1985.

[58] Karl S, Martinez Schramm J, Hannemann K. High enthalpy cylinder flow in HEG: A basis for CFD validation. AIAA paper 2003-4252; 2003.

[59] Olynick D, Chen Y-K, Tauber ME. Aerothermodynamics of the Stardust sample return capsule. J Spacecr Rockets 1999;36(3):442–62.

[60] Bariselli F, Torres E, Magin TE. State-specific catalytic recombination boundary condition for DSMC methods in aerospace applications. AIP Conf Proc 2016;1786(1):190009.